*Proceedings of the Twenty-ninth (2019) International Ocean and Polar Engineering Conference* **www.isope.org**
*Honolulu, Hawaii, USA, June 16-21, 2019*

*ISBN 978-1 880653 85-2; ISSN 1098-6189*

# Dynamic Analysis of Longline Aquaculture Systems with a Coupled 3D Numerical Model

*Longhuan Zhu*[1], *Kimberly Huguenard*[1], *David W. Fredriksson*[2]
[1]Department of Civil and Environmental Engineering, University of Maine, Orono, Maine, USA
[2]Department of Naval Architecture and Ocean Engineering, U.S. Naval Academy, Annapolis, Maryland, USA

## ABSTRACT

A 3D consistent mass-based model, cable model, is proposed to simulate the large deflection of the culture line structure. The 3D model couples the components of the entire aquaculture system. The simulations are performed with results compared with published data for suspended blades in both steady and oscillatory flow. Dynamics of a kelp longline system are studied for tidal currents scenarios. Results show that the longline tension follows water level to the peak at high tide and sensitive to water level in high tide. The non-parallel currents could enhance the tension as well as the deflection of the longline system.

KEY WORDS: Longline aquaculture systems; kelp; macroalgae model; cable dynamics.

## INTRODUCTION

Longline aquaculture systems are often used for the grow out of both shellfish and macroalgae products in protected waters. As this sector of the industry grows, more exposed sites will be considered. Longline gear components, however, will need to be optimized to survive extreme wave and current conditions while minimizing costs at exposed sites. These aquaculture structures may also have potential for shore protection as a kind of a living breakwater (Zhu and Zou, 2017). In each of these applications, numerical modeling tools are necessary that represent the dominating fluid and aquaculture system interaction processes. To analyze the dynamics of a mussel longline system, Raman-Nair et al (2008) developed a 3D numerical model coupling the longline and mussel dropper components. The longline was modeled as a lumped mass and tension-only springs system with the attached mussel culture components modeled as rigid cylinders. Cheng et al. (2017) developed a 2D numerical model for a kelp culture line modeled as a series of segments connected by hinges and springs to represent large deflections. A 2D consistent mass, cable model was proposed by Zhu et al. (2018) to simulate the dynamics of flexible kelp blades in waves. The results showed that the blade-induced vortices are asymmetric at both upstream and downstream positions of the flexible kelp model. The 2D models, however, are not able to simulate the dynamics of the longline system with non-parallel incident waves and currents because the motion of the culture line is 3D. Therefore, to build upon this work, the objectives of this paper are, (1) to propose a 3D form of the cable model to simulate the dynamics of the culture line, (2) incorporate hydrodynamic input for kelp blades, and (3) to couple the components of the entire aquaculture system based on the cable model. The coupled 3D model was then used to investigate the performance of a kelp longline system in tidal currents.

## METHODOLOGY

### Longline Configuration and Coordinate Systems

Typical longline aquaculture systems consist of anchors, mooring lines, buoys and longline that incorporate aquaculture components (Fig. 1). The aquaculture components can include densely grown kelp or shellfish droppers. Each component of the aquaculture system can be represented as a slender structure and modeled as a flexible cable. Flexible cable models have been used to analyze the dynamics of low-tensioned slender structures such as steel cables (e.g., Howell, 1992; Trianrafyllou, 1994; Tjavaras et al., 1998), risers (Chatjigeorgiou, 2008), mooring lines (e.g., Li et al, 2018), and vegetation (Zhu et al., 2018). To apply the cable model for a longline aquaculture system, two coordinate systems are employed including: (1) the global Cartesian coordinate system $(\hat{\imath}, \hat{\jmath}, \hat{k})$ and (2) the local Lagrangian coordinate system $(\hat{t}, \hat{n}, \hat{b})$ with $\hat{t}$ direction along the slender structure and moving with the structure.

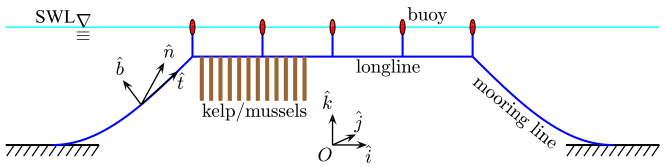


Fig. 1: Longline configuration and coordinate systems including the global Cartesian coordinate system $(\hat{\imath}, \hat{\jmath}, \hat{k})$ and a local Lagrangian coordinate system $(\hat{t}, \hat{n}, \hat{b})$.

The cable model requires a rotation matrix $(\boldsymbol{C})$. The rotation matrix $(\boldsymbol{C})$ transforms variables between coordinate systems using the Euler principle rotation theorem with an angle $(\alpha)$ about a unit vector $\vec{l} = [l_x \quad l_y \quad l_z]^T$ (Junkins and Turner, 1986). In the transformation, the four Euler parameters $\left(\vec{\beta} = [\beta_0 \quad \beta_1 \quad \beta_2 \quad \beta_3]^T\right)$ are defined as

$$\vec{\beta} = \left[\cos\frac{\alpha}{2} \quad l_x \sin\frac{\alpha}{2} \quad l_y \sin\frac{\alpha}{2} \quad l_z \sin\frac{\alpha}{2}\right]^T, \tag{1}$$

such that the rotation matrix can be written as

$$\boldsymbol{C} = \begin{bmatrix} \beta_0^2+\beta_1^2-\beta_2^2-\beta_3^2 & 2(\beta_1\beta_2+\beta_0\beta_3) & 2(\beta_1\beta_3-\beta_0\beta_2) \\ 2(\beta_1\beta_2-\beta_0\beta_3) & \beta_0^2-\beta_1^2+\beta_2^2-\beta_3^2 & 2(\beta_2\beta_3+\beta_0\beta_1) \\ 2(\beta_1\beta_3+\beta_0\beta_2) & 2(\beta_2\beta_3-\beta_0\beta_1) & \beta_0^2-\beta_1^2-\beta_2^2+\beta_3^2 \end{bmatrix}. \quad (2)$$

The dynamics of each slender structure is solved within local Lagrangian coordinate systems. To couple the aquaculture system components, the variables at each joint are transformed to the global coordinate system to establish boundary conditions. The aquaculture components (e.g., aggregate kelp blades, mussel droppers) are also modeled as slender structures.

## Governing Equations

The dynamics of each of the slender structure components are formulated from the same set of governing equations. The free-body diagram for a differential segment of the slender structure with initial unstretched length $ds$ at position $\vec{R}$ is shown in Fig. 2. The position vector $\vec{R}$ is a function of the distance along the blade structure ($s$) and time ($t$).

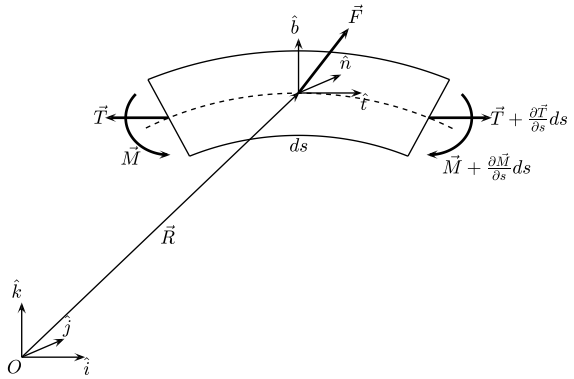


Fig. 2: The free-body diagram for segment $ds$ at position $\vec{R}$ with the global Cartesian coordinate system $(\hat{\imath},\hat{\jmath},\hat{k})$ and the local Lagrangian coordinate system $(\hat{t},\hat{n},\hat{b})$. The internal force is denoted by $\vec{T}$, the internal momentum denoted by $\vec{M}$, and the external force is denoted by $\vec{F}$.

The governing equations for the dynamics of the segment are given by

$$\rho\frac{\pi d^2}{4}\left(\frac{\partial\vec{V}}{\partial t}+\vec{\omega}\times\vec{V}\right)=\frac{\partial\vec{T}}{\partial s}+\vec{\Omega}\times\vec{T}+(1+\epsilon)\vec{F}, \quad (3)$$

$$\frac{1}{(1+\epsilon)^2}\frac{\partial\vec{M}}{\partial s}+\frac{1}{(1+\epsilon)^2}\vec{\Omega}\times\vec{M}+(1+\epsilon)\hat{t}\times\vec{T}=0, \quad (4)$$

and

$$\frac{\partial\epsilon}{\partial t}\hat{t}+(1+\epsilon)\vec{\omega}\times\hat{t}=\frac{\partial\vec{V}}{\partial s}+\vec{\Omega}\times\vec{V}, \quad (5)$$

where $\rho$ is the structure density, $d$ is the equivalent diameter of the structure, $\vec{V}=u\hat{t}+v\hat{n}+w\hat{b}$ is the velocity of the segment, $\vec{\omega}$ is the angular velocity of the local Lagrangian coordinate system with respect to the global Cartesian coordinate system, $\vec{T}=T\hat{t}+S_n\hat{n}+S_b\hat{b}$ is the internal force including tension and shear, $\epsilon$ is the strain, $\vec{F}$ is the external force, $\vec{M}=M_t\hat{t}+M_n\hat{n}+M_b\hat{b}$ is the internal momentum, and $\vec{\Omega}=\Omega_1\hat{t}+\Omega_2\hat{n}+\Omega_3\hat{b}$ is the Darboux vector interoperating the torsion and curvature of the structure. The relationship between $\vec{M}$ and $\vec{\Omega}$ is given by $M_t=GI_p\Omega_1$, $M_n=EI\Omega_2$, and $M_b=EI\Omega_3$, where $GI_p$ is the torsional stiffness and $EI$ is the bending stiffness of the structure. The tension $T$ and the strain $\epsilon$ are related by the tension-strain relation, where $\epsilon=T/(E\pi d^2/4)$ and $E\pi d^2/4$ is the axial stiffness. The angular velocity $\vec{\omega}$ and Darboux vector $\vec{\Omega}$ are obtained by

$$\begin{bmatrix}0\\ \vec{\omega}\end{bmatrix}=\boldsymbol{B}^{-1}\cdot\frac{\partial\vec{\beta}}{\partial t} \quad (6)$$

and

$$\begin{bmatrix}0\\ \vec{\Omega}\end{bmatrix}=\boldsymbol{B}^{-1}\cdot\frac{\partial\vec{\beta}}{\partial s}, \quad (7)$$

respectively, where,

$$\boldsymbol{B}=\frac{1}{2}\begin{bmatrix}\beta_0 & -\beta_1 & -\beta_2 & -\beta_3\\ \beta_1 & \beta_0 & -\beta_3 & \beta_2\\ \beta_2 & \beta_3 & \beta_0 & -\beta_1\\ \beta_3 & -\beta_2 & \beta_1 & \beta_0\end{bmatrix} \quad (8)$$

and $\boldsymbol{B}^{-1}=4\boldsymbol{B}^T$. Removing the terms involving time, the governing equations can be reduced to the case for static equilibrium.

***External Forces.*** The external forces include weight, buoyancy and hydrodynamic drag and added mass. The weight and buoyancy of the segment are given by $\vec{W}=-\rho g\pi d^2/4\,\hat{k}$ and $\vec{B}=\rho_w g\pi d^2/4\hat{k}$, respectively, where $g$ is the gravitational acceleration and $\rho_w$ is the water density. Based on Morison equations (Morison, 1950), the hydrodynamic forces can be expressed in drag forces ($\vec{F}_d$), added mass forces ($\vec{F}_a$), and virtual buoyancy (Froude–Krylov force, $\vec{F}_v$). Given the flow velocity $\vec{V}_w=u_w\hat{t}+v_w\hat{n}+w_w\hat{b}$, the hydrodynamic forces are expressed as

$$\vec{F}_d=-\frac{1}{2\sqrt{1+\epsilon}}\rho_w d\pi C_{dt}|u-u_w|(u-u_w)\,\hat{t}-\frac{1}{2\sqrt{1+\epsilon}}\rho_w dC_{dn}\sqrt{(v-v_w)^2+(w-w_w)^2}(v-v_w)\hat{n}-\frac{1}{2\sqrt{1+\epsilon}}\rho_w dC_{dn}\sqrt{(v-v_w)^2+(w-w_w)^2}(w-w_w)\hat{b}, \quad (9)$$

$$\vec{F}_a=-\frac{\rho_w\pi d^2C_a}{4(1+\epsilon)}\frac{\partial(v-v_w)}{\partial t}\hat{n}-\frac{\rho_w\pi d^2C_a}{4(1+\epsilon)}\frac{\partial(w-w_w)}{\partial t}\hat{b}, \quad (10)$$

and

$$\vec{F}_v=\rho_w\frac{\pi d^2}{4}\frac{\partial u_w}{\partial t}\hat{t}+\rho_w\frac{\pi d^2}{4}\frac{\partial v_w}{\partial t}\hat{n}+\rho_w\frac{\pi d^2}{4}\frac{\partial w_w}{\partial t}\hat{b}, \quad (11)$$

where $C_{dt}$ and $C_{dn}$ are the drag coefficients, and $C_a$ is the added mass coefficient.

## Boundary Conditions

***Anchors.*** Anchor positions at the end of the mooring lines are modeled as simple-supported nodes where the displacement, velocity and momentum are $\vec{0}$.

***Buoys.*** Buoys are modeled as rigid bodies. The supporting line is assumed to be hinged at the center of the buoy so that the momentum transformation is ignored. The motion of the buoy is governed by

$$m_B\frac{d\vec{V}_B}{dt}=\vec{W}_B+\vec{B}_B+\vec{F}_{dB}+\vec{F}_{aB}+\vec{F}_{vB}-\vec{T}_B, \quad (12)$$

where $m_B$ is the buoy mass, $\vec{V}_B$ is the buoy velocity, $\vec{W}_B$ is the weight, $\vec{B}_B$ is the buoyancy of the buoy, $\vec{F}_{dB}$ is the drag force, $\vec{F}_{aB}$ is the added9

mass force, $\vec{F}_{vB}$ is the virtual buoyancy, and $\vec{T}_B$ is the internal force of the supporting line. The formulas for calculating $\vec{F}_{dB}$, $\vec{F}_{aB}$ and $\vec{F}_{vB}$ are referred to Eqs. 9~11. The internal force ($\vec{T}$) of the supporting line at the end attached to a buoy is determined by Eq. 12. The velocity of the line should be equal to the velocity of the buoy. The momentum is set to be $\vec{0}$.

***Connections*.** The joint connecting the mooring lines, longline, and supporting lines can be assumed rigid or hinged. For rigid connection, the displacement and velocity are equal, and the total force and momentum are $\vec{0}$. For hinged connection, the displacements and velocities of the lines at the joint are equal, the total force and momentum at the joint are both $\vec{0}$. The connection joining the longline and the aquaculture components are assumed to be continuous and the culture line assumed to be attached to the longline without momentum transformation. Therefore, the displacements and velocities of longline and hanging structure are equal, the total force at the joint is $\vec{0}$, the momentum and angles of the longline at the joint are equal, and the momentum of the hanging structure is $\vec{0}$.

## Differential Equation Solver

The governing equations for each of the aquaculture components are coupled into a system of partial differential equations through the boundary conditions for connections. The system of partial differential equations is discretized using a finite difference method with box method scheme (Hoffman and Frankel, 1993; Chatjigeorgiou, 2008). The Newton-Raphson iteration method is used to solve the discretized nonlinear equations.

# DATA COMPARISONS

The model was compared with experiments for flexible blades in both steady and oscillatory flow.

## Flexible Blades

***Steady flow*.** The cable model developed was used to replicate experiments by Dijkstra and Uittenbogaard (2010) in steady flow. The top end of the model blades was clamped. The dimensions of the cross-section of the blades as well as the physical properties are shown in Table 1.

Table 1. Geometrical and physical properties of the model blades (modified from Table 1 of Dijkstra and Uittenbogaard, 2010).

| Blade | Very flexible (FR) | Tie wrap (TW) |
|---|---|---|
| Material | PVC | Nylon 66 |
| $E$ (N m$^{-2}$) | $1.60 \times 10^9$ | $1.06 \times 10^9$ |
| Thickness (mm) | 0.178 | 1.009 |
| Width (mm) | 5.0 | 4.8 |
| $I$ (m$^4$) | $2.30 \times 10^{-15}$ | $4.11 \times 10^{-13}$ |
| Density (kg m$^{-3}$) | 975 | 1080 |

In both the model and experiment, the blade is fixed at the top end and suspended in the water. Blades having lengths of 0.127, 0.177 and 2.27 m were simulated at the flow velocities of 0.02, 0.05, 0.081, 0.114, 0.183, 0.250, 0.318, and 0.386 m/s. To compare with the simulations by Dijkstra and Uittenbogaard (2010), the same drag coefficients are used in the cable model. The drag coefficients are given by (Hoerner, 1965; Dijkstra and Uittenbogaard, 2010)

$$C_{dt} = 0.018 f \sin\lambda, \tag{13}$$

and

$$C_{dn} = \min(2\cos\lambda + 0.1\tan\lambda, 2\pi), \tag{14}$$

where, $f$ is the ratio between the wetted area and the cross section and set as 2.8 to be the same in Dijkstra and Uittenbogaard (2010), and $\lambda$ is the angle between the blade and the vertical direction.

To quantify the performance of the numerical simulations, the difference between simulated and observed postures are introduced. The distance between the simulated point $(x_i, z_i)$ of the $i$th segment along the blade and the corresponding observed point $(x_{oi}, z_{oi})$ is defined as

$$d_i = \sqrt{(x_i - x_{oi})^2 + (z_i - z_{oi})^2}. \tag{15}$$

Therefore, the spatial averaged difference along the blade length normalized by the blade length ($L$) can be obtained

$$\widetilde{\langle d \rangle} = \sum_1^n d_i / nL, \tag{16}$$

where, $n$ is the number of segments, which is determined by the number of measured points. The posture comparisons are shown in Fig. 3 and the corresponding $\widetilde{\langle d \rangle}$s are show in Fig. 4.

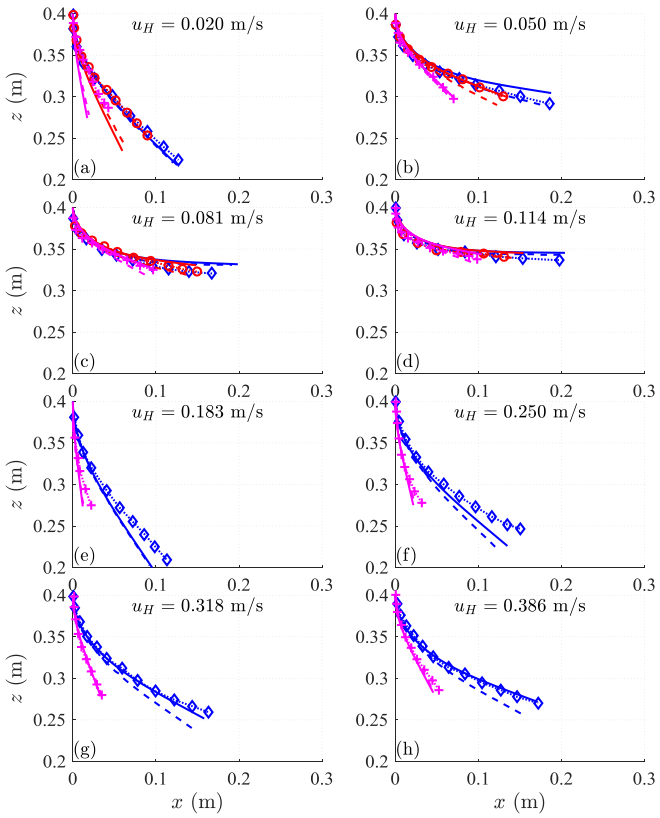


Fig. 3: Posture comparisons for (a~d) very flexible blade (FR) and (e~h) tie wraps (TW) with different lengths at four velocities. The lengths are 0.127, 0.177, and 0.227 m and denoted by magenta, red and blue, respectively. The measured data is denoted by crosses, circles, and diamonds, respectively. The simulations by Dijkstra and Uittenbogaard (2010) are denoted by dashed lines while the simulations by present

model are denoted by solid lines.

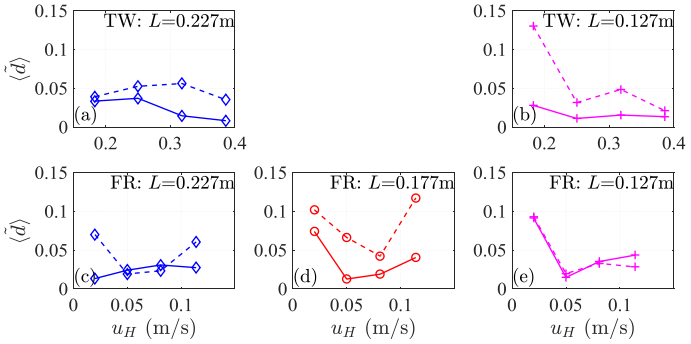


Fig. 4: The spatial averaged difference between the simulated postures and the observed postures for (a~b) tie wraps (TW) and (c~e) very flexible blade (FR) with different lengths. The lengths are 0.127, 0.177, and 0.227 m and denoted by magenta, red and blue, respectively. The $\widetilde{\langle d \rangle}$ simulations by Dijkstra and Uittenbogaard (2010) are denoted by dashed lines while that by the cable model are denoted by solid lines.

The cable model simulations show good agreement with the data with $\widetilde{\langle d \rangle} < 0.05$ except for the 0.177 and 0.127 m-long FR blades at the flow velocity of 0.02 m/s with $\widetilde{\langle d \rangle}$=0.07 (Fig. 4d) and $\widetilde{\langle d \rangle}$=0.09 (Fig. 4e), respectively. The $\widetilde{\langle d \rangle}$ produced by the cable model simulation is smaller than that by Dijkstra and Uittenbogaard (2010) except for the 0.227 m-long FR blade at the flow velocity of 0.05 m/s and 0.081 m/s, where the $\widetilde{\langle d \rangle}$ by cable model is slightly larger by 0.001 and 0.002, respectively, as shown in Fig. 4(c). Overall, the present model works well for simulating blade flexibility in steady flow.

***Oscillatory flow.*** Model simulations were also conducted to examine performance with oscillatory flow results from experiments described in Leclercq and de Langre (2018). In the physical model experiments, rectangular blades were cut from plastic sheets with a mass density of 895 kg m$^{-3}$. The blades were 0.2 m long, 0.02 m wide and 0.49 mm thick. The blade was clamped to a device that capable of oscillatory translations. The oscillatory translation moved in the horizontal direction with an amplitude of $A$ and angular frequency of $\sigma$. The relative flow velocity ($u_H \hat{\imath}_G$) is in the opposite direction of the oscillatory translation such that $u_H = -A\sigma \sin \sigma t$. The amplitude and angular frequency are normalized by the blade length ($L$) and the natural frequency of the blade ($T_s$), respectively, such that $\tilde{A} = A/L$ and $\tilde{\sigma} = \sigma T_s$, where $T_s = L^2\sqrt{m_a/EI}$ and $m_a$ is added mass per unit length. The amplitude $A$ ranges from 0.054 to 0.130 m and the frequency ranges from 0.21 to 1.08 Hz such that $\tilde{A} = 0.27$~$0.65$ and $\tilde{\sigma} = 2.3$~$12$. The added mass per unit length is $m_a = 0.314$ kg/m. The drag coefficient $C_{dn}$ is selected as 2 to be the same with Leclercq and de Langre (2018).

Simulations were conducted to replicate the oscillatory tests to assess the performance of the cable model for oscillatory flow. The amplitude of the blade tip end ($\tilde{X}_{\text{tip}}$) normalized by the blade length along $\tilde{\sigma}$ is shown in Fig. 5(a). For small-amplitude oscillatory flow with $\tilde{A} = 0.27$, The root-mean-square-error (rmse) of the simulations by cable model is 0.016, compared to that from Leclercq and de Langre (2018) with rmse=0.020. While for large-amplitude oscillatory flow with $\tilde{A} = 0.65$, the simulations by the cable model show a rmse=0.028. The rmse value could be attributed to the assumption of a constant drag coefficient. The drag coefficient should be reduced in a large-amplitude oscillatory flow while increased in a small-amplitude oscillatory flow. The selected tip excursions are compared for case A with $\tilde{A} = 0.27, \tilde{\sigma} = 0.23$ (Fig. 5b) and case B with $\tilde{A} = 0.65, \tilde{\sigma} = 12$ (Fig. 5c). The measured tip excursion for case A is asymmetric while the simulation by the cable model is more symmetric. For case B, the simulation of the tip excursion is in the similar amplitude with the measured tip excursion, but lower in the vertical direction. However, the model captures the characteristics of the tip excursion, which shows a figure eight ("∞").

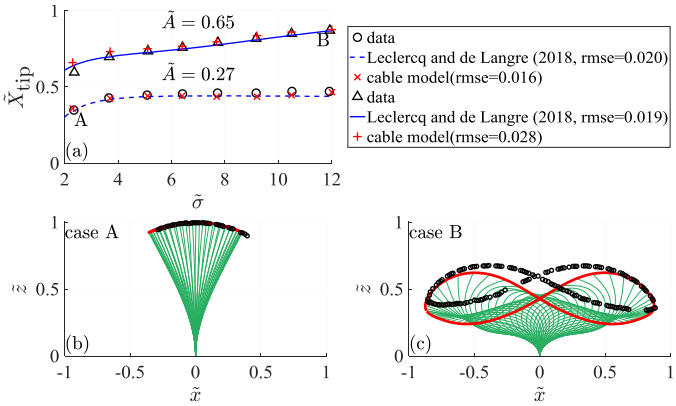


Fig. 5: Comparisons for the (a) amplitude of the deflection at the tip ($\tilde{X}_{\text{tip}}$) and (b-c) the tip excursions for case A ($\tilde{A} = 0.27, \tilde{\sigma} = 0.23$) and case B ($\tilde{A} = 0.65, \tilde{\sigma} = 12$). In (b) and (c), the measured tip excursion is denoted by black circles and the simulated tip excursion is denoted by red solid line.

## CASE STUDY

### Kelp Aquaculture Systems

A case study was conducted using parameters from a kelp longline that was deployed near Wood Island in the State of Maine, US, as shown in Fig. 6. The longline was 60 meters long, but only 30 meters kelp was grown on the western portion of the system. The general dimensions of the longline system and the detail component particulars are shown in Fig. 7. The water level for the initial configuration of the longline system was set at 8 m from in-situ measurements.

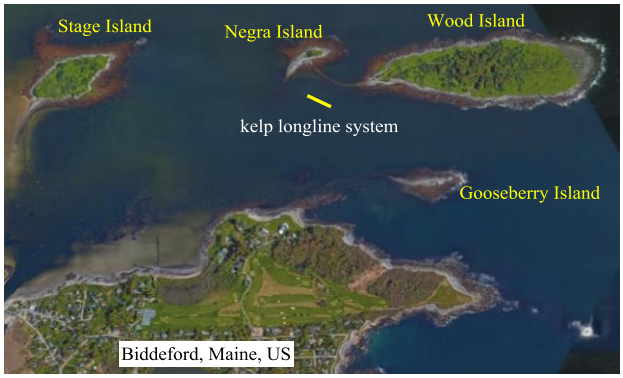


Fig. 6: Study site for the kelp longline system (modified from google satellite map). The approximated location of the kelp longline system is marked as yellow bar.

The kelp model employed in the computer program represents an aggregate of blades per meter of longline. The modulus $E$ was obtained by performing cantilever beam tests of kelp samples with measured tip deflections and second area moment calculated values of the measured cross-sections. These characteristics were obtained from 41 kelp subsamples taken from three locations along five separate blade samples. The geometric and material properties of the components are shown in

Table 2. Each component is modeled as a slender structure with the same length and an effective diameter such that the volumes are equal. This method matches the weight and buoyancy but changes the hydrodynamic properties. Work is presently being conducted to develop the "kelp" model. To show the utility of the modeling framework, however, general hydrodynamic coefficients of $C_{dn} = 1.2$ and $C_{dt} = 0.01$ are employed. The added mass coefficient is assumed to be $C_a = 1$.

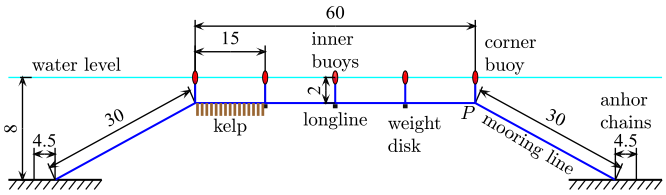


Fig. 7: General dimensions of the kelp longline system as well as the detail components. All the dimensions are in meters. The joint *P* connects the longline, the right corner buoy line and the mooring line.

Table 2. Geometrical and physical properties of the components.

| | Length $l$ (m) | Effective Diameter $d$ (m) | Density $\rho$ (kg/m$^3$) | Modulus $E$ (Pa) |
|---|---|---|---|---|
| Anchor chains | 4.5 | 0.02 | 7850 | $1.8\times10^{11}$ |
| Mooring lines | 30 | 0.01 | 1150 | $4\times10^{9}$ |
| Long-lines | 60 | 0.01 | 1150 | $4\times10^{9}$ |
| Buoy lines | 2 | 0.01 | 1150 | $4\times10^{9}$ |
| Inner buoys | 0.30 | 0.18 | 128 | - |
| Corner buoys | 0.35 | 0.29 | 80 | - |
| Weight disks | 0.15 | 0.18 | 2400 | - |
| Kelp | 0.43 | 0.14 | 1058 | $7.42\times10^{6}$ |

## Tidal Currents

The currents and water level were measured with an Acoustic WAve and Current (AWAC) profiling instrument. The instrument was set to measure only profiles at 0.5-meter bins. The east-going velocity component parallels to the longline dominates as shown in Fig. 8. To investigate the influences of the water level and currents, several cases were conducted with changing water levels associated with east-going velocities and north-going velocities of the currents.

## Results and Discussions

Simulations were performed with the AWAC data and system configuration (with kelp) parameters as input for the four cases WL (water level), WLEV (water level with east-going velocity), WLNV (water level with north-going velocity), and WLC (water level with currents). Selected reconfigurations of the longline system in one tidal cycle are shown in Fig. 9. The longline tension at the joint *P* associated with the displacements are shown in Fig. 10. The joint *P* connects the longline, right corner buoy line and mooring as shown in Fig. 7 and Fig. 9.

The tension follows the water level with smaller values at low tide and larger values at high tide. With an increasing submerged length of the buoys from low tide to high tide, the buoyancy increases such that the tension of the longline increases correspondingly. As shown in Fig. 10a, the tension for the first high tide with a water depth of 7.8 m at time $t_1$ (Fig. 10a) is 218 N while the tension for the following high tide with a water depth of 8.3m at time $t_2$ is 457N. The latter tension is more than

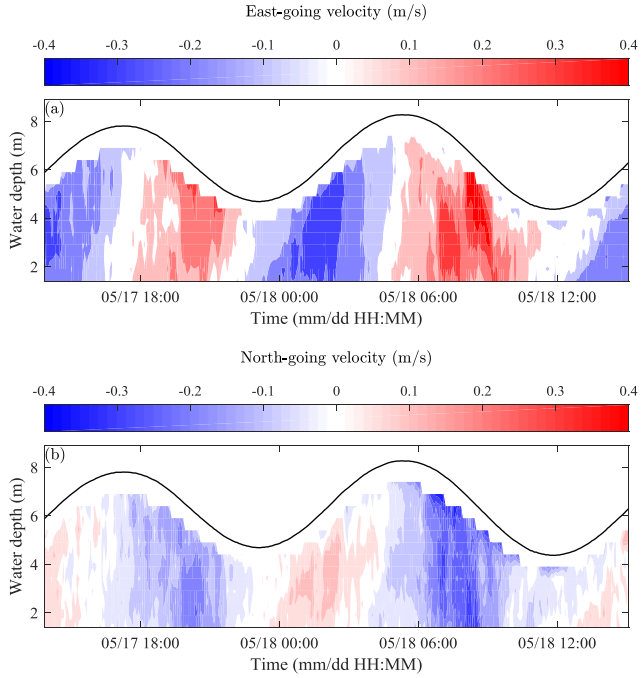


Fig. 8: Time series of (a) east-going velocity and (b) north-going velocity along water depth. The water level is denoted by black line.

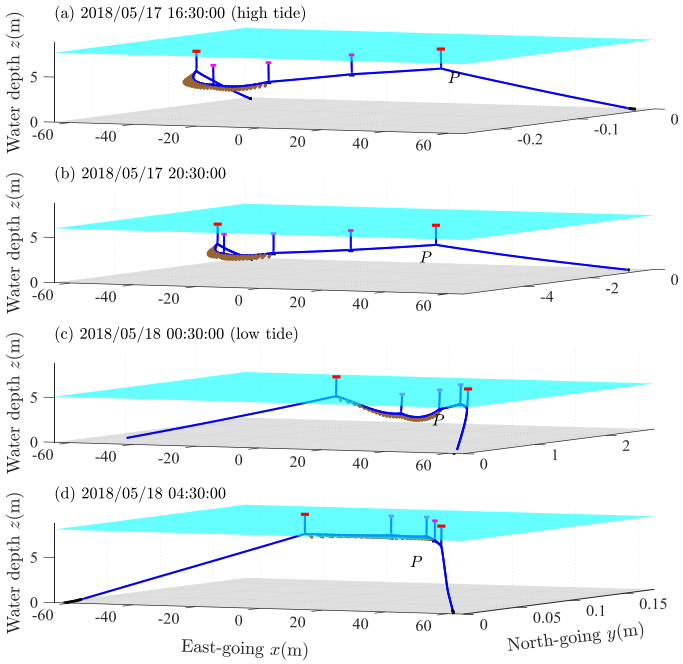


Fig. 9: Reconfigurations of the kelp longline system in one tidal cycle.

twice of the former although the water depth increases slightly by 0.5 m compared with the tidal range of 3.9 m. Because the longline system is tensioned at the initial configuration with a water depth of 8 m, the tension is more sensitive to water level change in high tide when the water depth is larger than the initial water depth. This suggests that the tension could increase dramatically in tidal surge. The east-going velocity has little influence on the tension. However, the north-going velocity perpendicular to longline impacts the tension significantly, especially during ebbing when the longline system become less

tensioned. For example, the tension with the north-going velocity (WLNV and WLC) is more than twice than that without north-going velocity (WL and WLEV) around the time of 7:00 on May 18th, as shown in Fig. 10a.

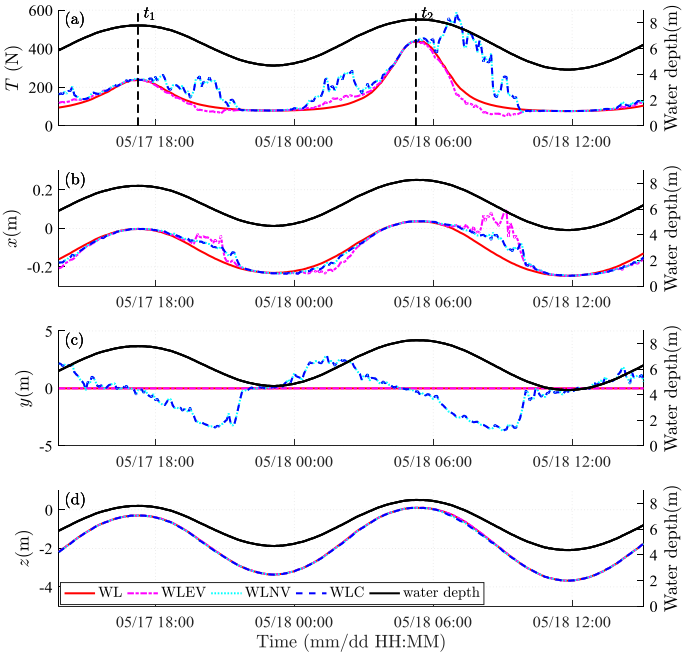


Fig. 10: (a) Tension ($T$) of the longline at joint $P$ that connects the longline, right corner buoy line and mooring line. (b) The east-west displacement ($x$), (c) the north-south displacement (y) and (d) the vertical displacement ($z$) of joint $P$. The results for cases WL (water level), WLEV (water level with east-going velocity), WLNV (water level with north-going velocity), and WLC (water level with currents) are denoted by red solid lines, magenta dash-dotted lines, cyan dotted lines, and blue dashed lines, respectively. The water level is denoted by black solid line. The vertical black dashed lines indicate time $t_1$ and $t_2$ for the high tides.

The three components of the displacements of the joint $P$ demonstrate different patterns as shown in Fig. 10(b~d). The east-west displacement ($x$) is less impacted from the currents in high tide because the longline system is high tensioned. The influence of the north-going velocity on the east-west displacement is small compared with that from the east-going velocity. The north-south displacement is 0 without north-going velocity components but significantly with north-going velocity. Following north-going velocity, the north-south displacements show a phase shift with the water level. Compared with the east-west displacement in the magnitude of decimeters, the north-south displacement has a magnitude in meters. The deflection of the longline is more serious under the action of the non-parallel velocity. The vertical displacements follow the water level without influence from the currents because the vertical component of water velocity is 0 and the joint moves with the buoy following water level.

## CONCLUSIONS

A 3D cable model was developed to simulate the large deflection characteristics of culture line structures that can consist of shellfish or macroalgae. Simulation results were compared with experiments for suspended flexible blades in both steady and oscillatory flow. The coupled 3D model was then used to investigate the dynamic performance of a longline system in tidal currents. Results show that the tension increases with water level to a peak at high tide. The tension could increase dramatically when the water level exceeds the initial water depth at which the longline system is deployed. This suggests that the longline system could face a high risk of failure in high water level such as tidal surge and waves. The results also demonstrate that the non-parallel currents not only increase the tension but also enhance the deflection of the longline system. To improve the performance, the longline system should be deployed parallel to the direction of dominated velocity. The future work will focus on the model comparison with the field data and the influences of the initial configuration on the dynamics of the longline system.

## ACKNOWLEDGEMENTS

This study was supported by National Science Foundation award #IIA-1355457 to Maine EPSCoR at the University of Maine.

## REFERENCES

Cheng, W., Sun, Z., and Liang, S. (2017). "Dynamic simulation of a kelp raft culture system under current," *Proc 27th Int Ocean and Polar Eng Conf*, San Francisco, ISOPE, 1452–1458.

Dijkstra, J. T., and Uittenbogaard, R. E. (2010). "Modeling the interaction between flow and highly flexible aquatic vegetation," *Water Resources Research*, 46(12).

Hoerner, S. F. (1965). *Fluid-Dynamic Drag*, Hoerner Fluid Dyn., Vancouver, B. C., Canada.

Hoffman, J. D., and Frankel, S. (1993). *Numerical methods for engineers and scientists*. McGraw-Hill, New York.

Howell, C. T. (1992). *Investigation of the dynamics of low-tension cables*. Ph.D. thesis Massachusetts Institute of Technology and Woods Hole Oceanographic Institution.

Junkins, J. L., and Turner, J. D. (1986). *Optimal spacecraft rotational maneuvers*. Elsevier.

Leclercq, T., and de Langre, E. (2018). "Reconfiguration of elastic blades in oscillatory flow," *Journal of Fluid Mechanics*, 838, 606-630.

Li, Y., Zhu, Q., Liu, L., and Tang, Y. (2018). "Transient response of a SPAR-type floating offshore wind turbine with fractured mooring lines," *Renewable Energy*, 122, 576-588.

Morison, J. R., Johnson, J. W., & Schaaf, S. A. (1950). "The force exerted by surface waves on piles," *Journal of Petroleum Technology*, 2(05), 149-154.

Raman-Nair, W., Colbourne, B., Gagnon, M., and Bergeron, P. (2008). "Numerical model of a mussel longline system: Coupled dynamics," *Ocean Engineering*, 35(13), 1372-1380.

Tjavaras, A. A., Zhu, Q., Liu, Y., Triantafyllou, M. S., & Yue, D. K. P. (1998). "The mechanics of highly-extensible cables," *Journal of Sound and Vibration*, 213(4), 709-737.

Trianrafyllou, M. (1994). "Cable mechanics for moored floating structures," *Proc of the 7th International Conference on the Behaviour of Offshore Structures (BOSS 1994)*, 2, 57-77.

Zhu, L., Huguenard, K., & Fredriksson, D. (2018). "Interaction between waves and hanging highly flexible kelp blades," *Proc 36th International Conference on Coastal Engineering*, 1(36), 31. doi:https://doi.org/10.9753/icce.v36.papers.31

Zhu, L., and Zou, Q. (2017). "Three-layer analytical solution for wave attenuation by suspended and nonsuspended vegetation canopy," *Proc 35th International Conference on Coastal Engineering*, 1(35), 27. doi:https://doi.org/10.9753/icce.v35.waves.27